Microsyst Technol (2012) 18:1045–1056
DOI 10.1007/s00542-012-1437-9

TECHNICAL PAPER

Sensing viscosity and density of glycerol–water mixtures utilizing a suspended plate MEMS resonator

Samir Cerimovic · Roman Beigelbeck · Hannes Antlinger · Johannes Schalko · Bernhard Jakoby · Franz Keplinger

Received: 18 August 2011 / Accepted: 18 January 2012 / Published online: 7 February 2012

Abstract A sensor suitable for online monitoring of viscosity and density of glycerol–water mixtures is presented. The device is based on Lorentz force excitation and features an integrated piezoresistive readout. The core sensing element is a rectangular vibrating plate suspended by four beam springs. Two of the plate-carrying springs comprise piezoresistors. With two additional resistors on the silicon rim they form a half Wheatstone-bridge. Through the conductive layer of the beam springs a sinusoidal excitation current is driven. In the field of a permanent magnet, the Lorentz force excites plate vibrations resulting in a bridge unbalance. We recorded both the frequency response of the amplitude and the phase of the bridge output. By evaluating the properties of the resonant system, it is possible to extract the glycerol percentage and, hence, the viscosity and the mass density of the mixtures.

This work is an extended version of the paper originally presented at SPIE Microtechnologies conference in Prague, Czech Republic (2011), published in: "Proceedings of SPIE", vol. 8066 80662E-1.

S. Cerimovic (✉) · J. Schalko · F. Keplinger
Institute of Sensor and Actuator Systems,
Vienna University of Technology,
Gusshausstr. 27-29, 1040 Vienna, Austria
e-mail: samir.cerimovic@tuwien.ac.at
URL: http://www.isas.tuwien.ac.at

R. Beigelbeck · J. Schalko
Institute for Integrated Sensor Systems,
Austrian Academy of Sciences,
Viktor Kaplan Str. 2,
2700 Wiener Neustadt, Austria

H. Antlinger · B. Jakoby
Institute for Microelectronics and Microsensors,
Johannes Kepler University Linz,
Altenberger Str. 69, 4040 Linz, Austria

List of symbols

A_0	Static plate deflection (m)
B	Flux density (T)
c_{glyc}	Glycerol concentration in the mixture (wt%)
D	Damping factor
E	Young's modulus (Pa)
f	Frequency (Hz)
f_0	Natural resonant frequency of the system without damping (Hz)
f_b	Frequency of the bridge supply voltage (Hz)
f_{ch}	Characteristic frequency (Hz)
f_e	Excitation frequency (Hz)
f_r	Measured resonant frequency (Hz)
h	Height of cantilever beams and plate (m)
k	Spring constant (N/m)
K_0, K_1	Modified Bessel functions of the third kind
i_e	Excitation current (A)
$\mathbf{i}_z$	Unity vector in z-direction
j	Imaginary unit
L	Total cantilever length (m)
$m'_{a,spring}$	Added mass per unit length of the springs (kg/m)
Q	Quality factor
$R_{1–4}$	Piezoresistors (Ω)
ΔR	Change of the resistance (Ω)
Re	Reynolds number
R_0	Resistance at zero stress (Ω)
t	Time (s)
u_b	Bridge supply voltage (V)
u_d	Bridge differential voltage (V)
$u_{d,comp}$	Compensated bridge differential voltage (V)
$u_{d,excit}$	Bridge differential voltage with excitation (V)
$u_{d,noexcit}$	Bridge differential voltage without excitation (V)

$u_{d,offset}$	DC offset of u_d (V)
u_e	Excitation voltage (V)
w	Cantilever width (m)
α	Mass damping parameter of Rayleigh damping model (1/s)
β	Stiffness damping parameter of Rayleigh damping model (s)
Γ	Hydrodynamic function
Γ'	Real part of Γ
Γ''	Imaginary part of Γ
Γ_{circ}	Hydrodynamic function for a beam with a circular cross-section
Γ_{rect}	Hydrodynamic function for a beam with a rectangular cross-section
γ	Viscous damping coefficient (kg/s)
γ'	Damping coefficient per unit length (kg/ms)
$\gamma'_{a,spring}$	Added damping coefficient per unit length of the springs (kg/ms)
η	Dynamic viscosity (Pas)
π	Mathematical constant
π_l	Longitudinal piezoresistance coefficient (Pa^{-1})
ρ	Mass density (kg/m^3)
σ_l	Longitudinal stress (Pa)
ϕ	Phase shift between excitation current and output signal (°)
ϕ_{comp}	Compensated phase shift (°)
ψ	Plate deflection (m)
Ω	Correction function
ω	Angular frequency of vibrations (s^{-1})

1 Introduction

Online monitoring of liquids is in many applications of particular importance. During the past two decades several efforts have been made to evaluate viscosity, mass density, permittivity, and thermal conductivity regarding their suitability as monitoring parameters (Jakoby and Vellekoop 2004; Kuntner et al. 2006; Kuntner 2008; Beigelbeck et al. 2011). While thermal conductivity measurements are traditionally utilized for gas sensing (e.g., gas chromatographs (Grob and Barry 2004)) and permittivity monitoring is commonly used in combination with capacitive-based readout mechanisms (e.g., fuel level indicators (Toth et al. 1997; Shi et al. 1991)), the focus of interest has clearly shifted to viscosity and mass density detection. This work covers the sensing of viscosity and mass density of glycerol–water mixtures.

Modern online monitoring systems focus on miniaturized, highly-integrated solutions. However, conventional laboratory equipment for viscosity measurement involve bulky rotating cylinders or cones (Viswanath et al. 2007) and can therefore not be miniaturized sufficiently. Additionally, most of these devices require manual liquid withdrawal which is time-consuming, error-prone, and barely compatible with autonomous monitoring processes. Compared to these apparatuses, miniaturized vibrating structures such as plates or cantilevers offer some decisive advantages. For example, their small size enables implementation in highly integrated systems with low power consumption. The latter facilitates autarkic wireless devices driven by a battery or an energy harvester.

A well-established way to determine the viscosity of liquids with a miniaturized sensor relies on thickness shear mode (TSM) resonators. They embody an AT-cut quartz disk contacted with electrodes on both faces (Kanazawa and Gordon 1985). Applying an AC voltage to the electrodes excites through the piezoelectric effect shear vibrations of the disk. When immersed in the sample liquid, this movement imposes a dominant shear strain in the surrounding liquid. This interaction is viscosity dependent and attenuates the resonator vibration which can be detected by evaluating the frequency response of the impedance between the quartz electrodes (Martin et al. 1991). Beside small size and low cost, commonly used TSM resonators are distinguished by high mechanical stability. However, their operational frequency range in the MHz regime yields results that are not always directly comparable to those received from conventional viscometers as they usually measure at steady state or low-frequency motion. Due to the small penetration depth of the involved shear wave, typically in the (sub)micrometer range, only a thin film of liquid is probed. This has a severe impact on the obtained results when complex liquids (e.g., emulsions) are sensed (Riesch et al. 2008). Furthermore, the achievable vibration amplitudes are small requiring sophisticated readout techniques and circuitries. On the contrary, structures like vibrating beams, bridges, or membranes operate at lower frequencies and higher amplitudes. Therefore, they are more suitable for measuring complex and non-Newtonian liquids. The beams can be easily implemented in silicon micromachining technology (Riesch et al. 2007) or alternatively by utilizing polymer foils (Reichel et al. 2008). Notably, the latter technology is also suitable for the realization of vibrating membranes that can be embedded in microfluidic systems (Reichel et al. 2009). However, resonating beam or membrane structures often suffer from the absence of an integrated readout mechanism. Accordingly, the detection has to be implemented by spatially separated components limiting the usability and the application area of such devices. In case of an external optical readout (e.g., Nabil et al. 2001), the micromachined structures commonly vibrate in an out-of-plane mode. As a result, significant damping related to compressional waves (Beigelbeck and Jakoby 2004) leads to small vibration amplitudes and low Q-factors

associated with a pure signal-to-noise ratio (SNR). Induction-based integrated readout principles are typically used in combination with Lorentz force excited devices (Lucklum and Jakoby 2008). Again, a low SNR often hampers a wider measurement range.

The presented resonant MEMS sensor aims at improving the quality factor of the vibrating system. The device relies on Lorentz force excitation and features an integrated piezoresistive readout. The core sensing element is a rectangular, in-plane vibrating plate suspended by four beam springs. For thin plates, mainly shear waves are excited in the liquid nearby the plate. Consequently, the plate contribution to the damping of the sensor vibration is low. Furthermore, the plate increases the moving mass of the sensor, and, hence, also the quality factor of the resonant system. This improves the SNR of the sensor output significantly.

We chose glycerol–water mixtures as test liquids because they are inexpensive, non-toxic, easy to handle, and feature a well-defined dependence between glycerol concentration and mass density and viscosity. Glycerol is widely used in the food industry as a humectant, solvent, and sweetener. It is therefore important to have a sensor allowing online monitoring of the glycerol concentration. Nevertheless, the sensing principle is not limited to glycerol–water mixtures and, therefore, the device can be utilized for viscosity and density monitoring of arbitrary liquids in the viscosity range below 100 mPas.

2 Sensor design

Figure 1 depicts the schematic of the sensor device. The rectangular silicon plate measures 100 × 100 × 20 µm^3. Each supporting beam spring is 5 µm wide, 20 µm high, and 450 µm long. The beams bear a 500 nm thin conductive aluminum layer. In the field of a permanent magnet (flux density $\boldsymbol{B} = -320\ \mathrm{mT}\mathbf{i}_z$, where $\mathbf{i}_z$ is a unity vector in z-direction), the sinusoidal current $i_e(t)$ excites lateral deflections of the springs leading to time-harmonic in-plane oscillations of the suspended plate.

The sensor is fabricated on a silicon-on-insulator (SOI) wafer. The device layer is p-doped silicon which is inherently piezoresistive. The sensor utilizes this effect for the readout of the plate deflection. The ends of two beam springs are forked. One prong carries the metal layer for the excitation current while the other one forms a piezoresistive element (Fig. 2). The resistor dimensions are 50 × 3 × 50 µm^3 with a typical electric resistance of a few kΩ. These resistors (R_3 and R_4, Fig. 1) accompanied with two additional resistors placed on the silicon rim (R_1 and R_2) form a half Wheatstone bridge. Due to plate vibrations, the piezoresistors R_3 and R_4 are subjected to either compressive or tensile stress. This changes their electric resistance resulting in a bridge unbalance. As output signal we analyze the differential voltage $u_d(t)$.

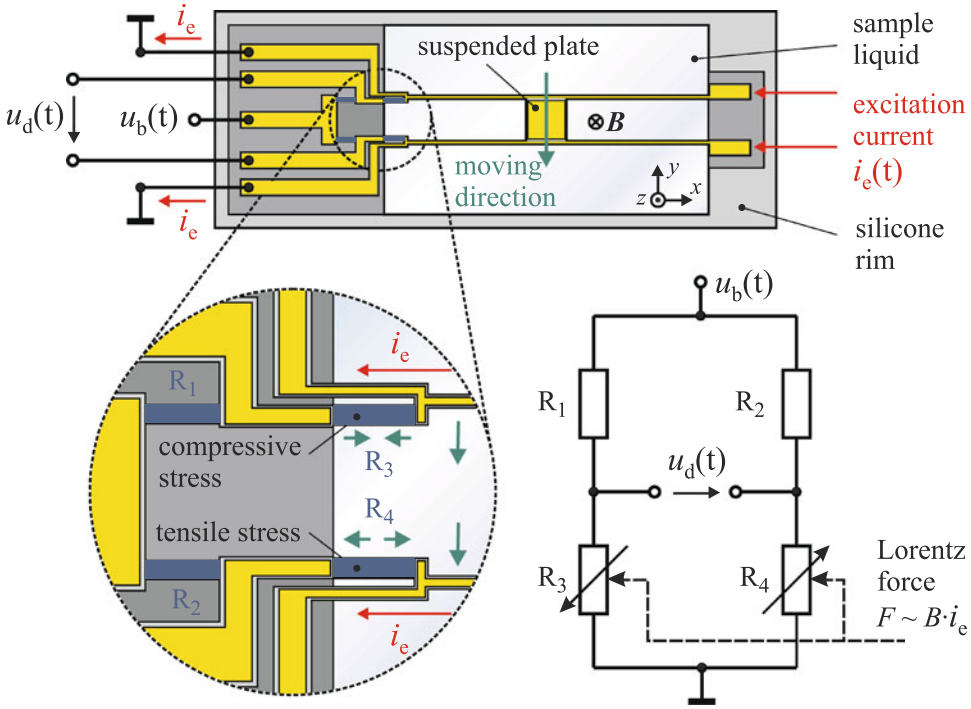

Fig. 1 Schematic of the sensor device illustrating suspended plate and piezoresistive readout. The plate vibrations are excited by the Lorentz force. The piezoresistors $R_{1–4}$ form a Wheatstone bridge supplied by the voltage u_b. The resistors R_3 and R_4 are subjected to alternating compressive and tensile stress due to the plate deflection

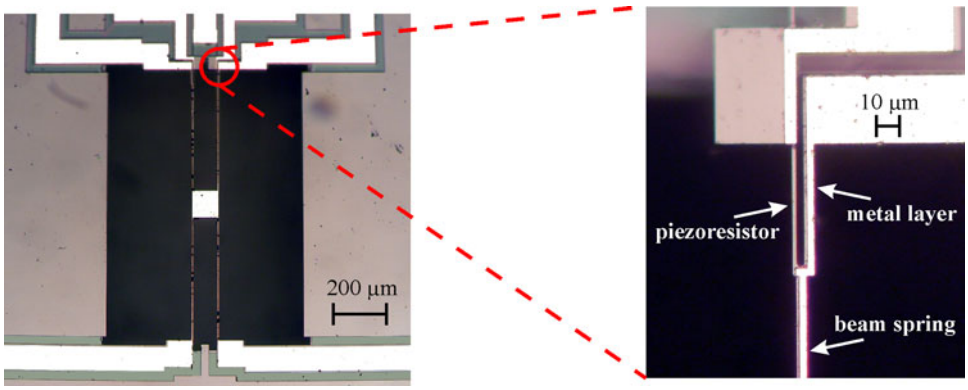

Fig. 2 Photomicrograph of the suspended plate sensor. The magnified image shows the forked end of one beam spring. One prong carries a conductive layer for the excitation current while the other one forms a piezoresistive element

3 Sensor fabrication

The sensor device is fabricated with a three-mask process (Fig. 3). A 4-inch (100) oriented SOI wafer serves as basic substrate. The thickness of the device layer, the buried oxide layer, and the handle layer are 20, 2, and 350 µm, respectively. The device silicon layer was p-doped featuring a typical resistivity of 0.2 Ωcm. Both sides of the wafer were coated by the vendor with thermally grown silicon dioxide (SiO_2) and low pressure chemical vapor deposited (LPCVD) silicon-nitride (Si_3N_4) featuring a thickness of 250 and 80 nm, respectively (Fig. 3a). The sensor

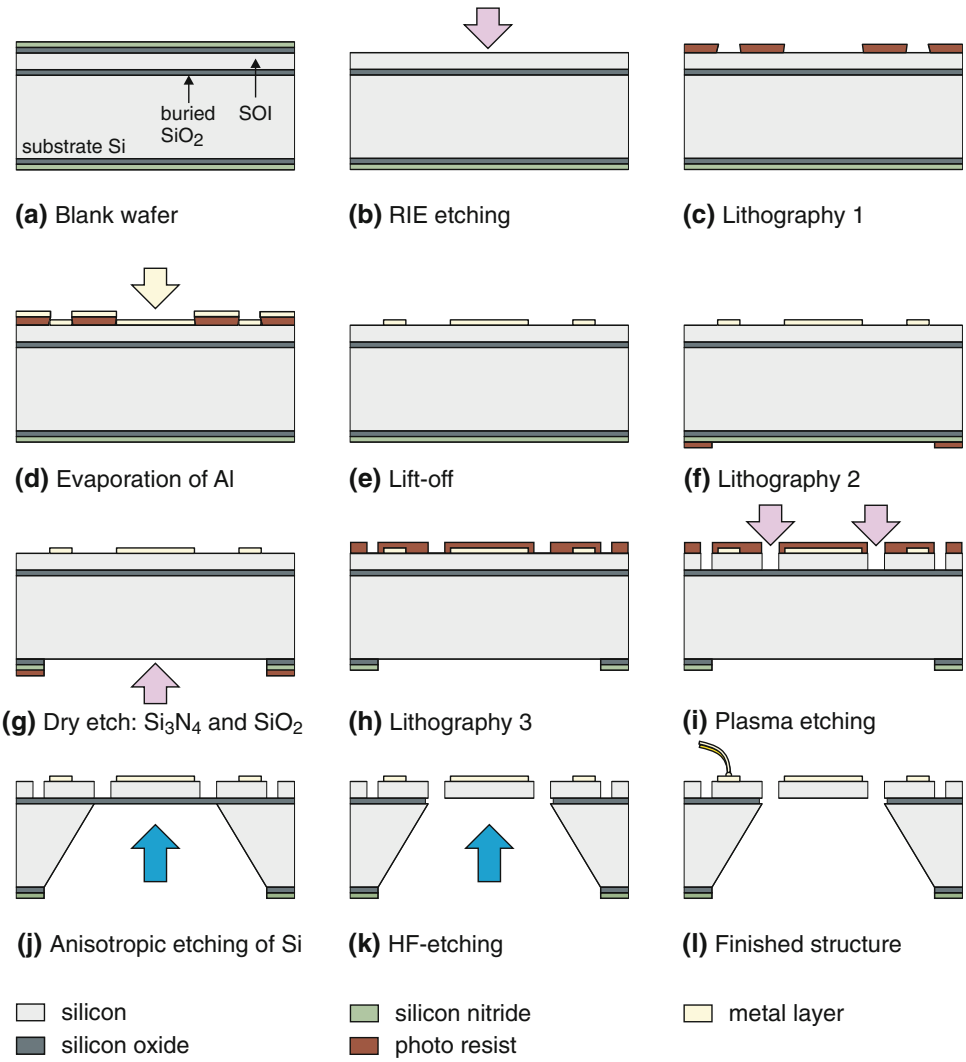

Fig. 3 Process flow diagram of the sensor fabrication

manufacturing started with the removal of the top side coating by reactive ion etching (RIE, Fig. 3b). The next step comprised a first photolithographic process (Fig. 3c) and a high-vacuum vapor-deposition of a 500 nm aluminum layer (Fig. 3d). This layer was patterned using lift-off technique (Fig. 3e) to form the electrical connections. Subsequent vacuum annealing was required to establish ohmic contacts between the metal layer and the silicon. The second photolithography was applied at the wafer backside to pattern the SiO_2 and Si_3N_4 double-layer (Fig. 3f). The blank areas were then dry etched using RIE (Fig. 3g). The resulting openings were made in preparation for the later KOH etching process. After the last photolithography (Fig. 3h), the plate and springs, the piezoresistors, and the conducting paths were formed by deep reactive ion etching (DRIE) of the device layer (Fig. 3i). Next, the wafer was protected on top by a special wafer holder and inserted into a solution of 80 wt% KOH at 80°C in order to etch the bulk silicon from the back side. The buried oxide layer stops the etching process (Fig. 3j). Subsequently, the suspended plate and the springs were released by wet etching with buffered hydrofluoric acid (Fig. 3k). After wafer dicing, the sensor device was die-bonded on small printed circuit board (PCB) and the electrical connections from chip to PCB were established by gold wire-bonding (Fig. 3l). Finally, the wire bonds were protected by an epoxy compound.

4 Modeling and simulations

In order to estimate the sensor characteristic for different fluid loads and to investigate the influence of design variations on the sensor behavior, sensor modeling and comprehensive simulations are necessary. Pure numerical simulations utilizing finite element method (FEM) are inappropriate in this case. Owing to high aspect ratios of some elements on the device layer and a rather complex interaction between liquid and mechanical parts accompanied with the piezoresistive effect, a sufficiently accurate FEM modeling would require high computing and memory capacity (Jakoby 2008). On the other hand, simplified analytical modeling yields results deviating up to 30% from the measured values (Riesch 2009).

In this paper, we present a semi-numerical approach that combines analytical and numerical modeling. Figure 4 shows the geometry of the 3D-FEM model. In order to reduce the number of mesh elements, the silicone rim with the additional piezoresistors was omitted. Length and height of the model elements agree with the values specified in the sensor design chapter. However, the width of the springs and piezoresistors was reduced to 20% in total (10% for each lateral wall, i.e., the springs are now 4 μm and the resistor 2.4 μm wide) to account for underetching during the DRIE process (Fig. 3i). The underetching correlates to specific process parameters and increases with the etching depth. By measuring the top and the bottom width of the cantilever, a mean value of 20% underetching was found as a good approximation. The model involves two application modes. The first one calculates the current distribution in the conductive layer. These results are then used to impose the acting Lorentz force on the vibrating structure. The liquid-structure interaction was implemented as additional mass and damping to the springs and the plate. The required parameters are gained utilizing an analytical model of the rectangular vibrating cantilever. The model is valid if the vibration amplitudes are far smaller than the beam geometry, the surrounding liquid is assumed to behave incompressible, the beam cross-section is uniform over the entire length, and the beam length greatly exceeds its nominal width. All these requirements are fulfilled in our case.

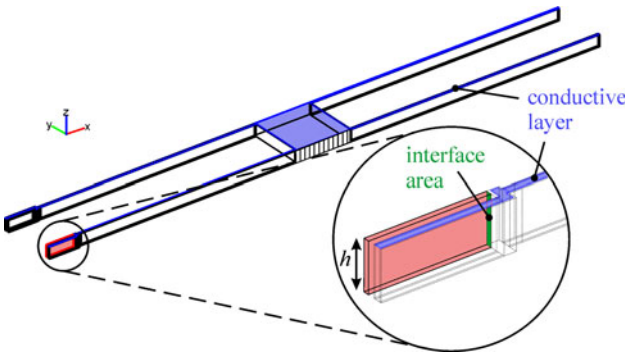

Fig. 4 Geometry of the 3D-FEM model. The inset shows the forked end of one spring with the piezoresistor (*highlighted area*) and the interface area where the stress was evaluated. The height of the device layer is $h = 20$ μm

To account for interaction of the four sensor springs with the surrounding liquid, the hydrodynamic function $\Gamma(\omega)$ must be calculated at first. The exact analytical result for $\Gamma(\omega)$ for a beam with a circular cross-section is given by (Sader 1998)

$$\Gamma_{\mathrm{circ}}(\omega) = 1 + \frac{4\mathrm{j}K_1(-\mathrm{j}\sqrt{\mathrm{jRe}})}{\sqrt{\mathrm{jRe}}K_0(-\mathrm{j}\sqrt{\mathrm{jRe}})}, \tag{1}$$

where j is the imaginary unit, $\mathrm{Re} = \rho\omega h^2/(4\eta)$ is the related Reynolds number, and K_0 and K_1 are the modified Bessel functions of the third kind. The density and viscosity of the liquid are denoted by ρ and η, respectively, whereas ω is a characteristic angular frequency of the vibration and h is the height of the cantilever beam (i.e., the height of the wafer device layer, Fig. 4 inset). The Reynolds numbers for the used test liquids range from 0.01 to 10 and depend mainly on the viscosity η. The rectangular cross-section of the

sensor springs can be taken into account by multiplying (1) with an appropriate correction function $\Omega(\omega)$ as follows

$$\Gamma_{\text{rect}}(\omega) = \Gamma_{\text{circ}}(\omega) \cdot \Omega(\omega). \tag{2}$$

The exact expression of the complex function $\Omega(\omega)$ is stated in Sader (1998). Using the hydrodynamic function, we can now calculate the added mass per unit length of the springs due to liquid loading (Riesch 2009)

$$m'_{\text{a,spring}} = \rho \frac{\pi}{4} h^2 \Gamma', \tag{3}$$

where Γ' is the real part of the hydrodynamic function. Note that the added mass is frequency dependent. With respect to its large lateral surface, the springs vibrate out-of-plane. Such a vibration mode generates a velocity field in the liquid that is associated with high damping. This damping was accounted for by using a Rayleigh damping model where the mass damping parameter α was set to zero and the stiffness damping parameter was given by

$$\beta = \frac{\gamma}{k} = (\gamma' L) \cdot \frac{L^3}{32 w^3 h E}. \tag{4}$$

Here, γ denotes the viscous damping coefficient and $E = 169$ GPa is the Young's modulus of silicon in [110] direction (Hopcroft et al. 2010). In Eq. (4) two supporting springs forming one side of the H-shaped sensor were modeled as one long doubly-clamped, uniformly loaded beam cantilever with a spring constant of $k = 32 w^3 h E / L^3$, where $w = 4$ µm is the cantilever width and $L = 2 \times 450$ µm is the total cantilever length. The added damping coefficient per unit length of the springs γ' can be calculated using the imaginary part of the hydrodynamic function Γ''

$$\gamma'_{\text{a,spring}} = \rho \frac{\pi}{4} h^2 \omega \Gamma''. \tag{5}$$

Contrary to the springs, the suspended plate vibrates in an in-plane mode. Thus, mainly shear waves associated with a low damping of the plate are excited in the surrounding liquid. It can be shown (Riesch 2009) that the major part of additional mass and damping due to liquid interaction stems from the vibrating springs. Therefore, we only considered the front face of the rectangular plate which vibrates in an out-of-plane mode (hatched area in Fig. 4) and used Eq. (3) multiplied with a plate length to calculate the additional mass. For reasons of simplification, all other effects that influence the plate added mass as well as the added damping of the plate were neglected.

On the p-doped device layer of the SOI wafer, the piezoresistors were aligned in the [110] direction. In this case, the change of the resistance due to applied stress reads

$$\Delta R = \pi_l \sigma_l R_0, \tag{6}$$

where R_0 is the resistance at zero stress and the longitudinal piezoresistance coefficient amounts to $\pi_l = 71.8 \cdot 10^{-11}$ Pa^{-1}. The longitudinal stress σ_l was calculated by evaluating the average force in x-direction at the interface between the piezoresistor and the spring (indicated in the inset of Fig. 4). Figure 5 illustrates the dependence of the resistance change on the frequency of the excitation current. The highest resonant frequency and the quality factor were achieved when the device is operated in air (i.e., approximately no viscous damping). If the sensor is immersed in a liquid, the resonant frequency is shifted to the lower values and the quality factor decreases depending on the viscosity and the mass density of the liquid. As an appropriate output quantity, the quality factor, the resonant frequency or, alternatively, the inflection point of the phase characteristic can be utilized. The exact evaluation of the simulation results will be presented below in the comparison with measurement results.

5 Device operation in air

The sensor was first characterized in air, i.e., for negligible viscous damping. Due to in-plane vibrations, the stroboscopic planar mode of a microsystem analyzer was utilized for the deflection measurement of the plate. The sensor was

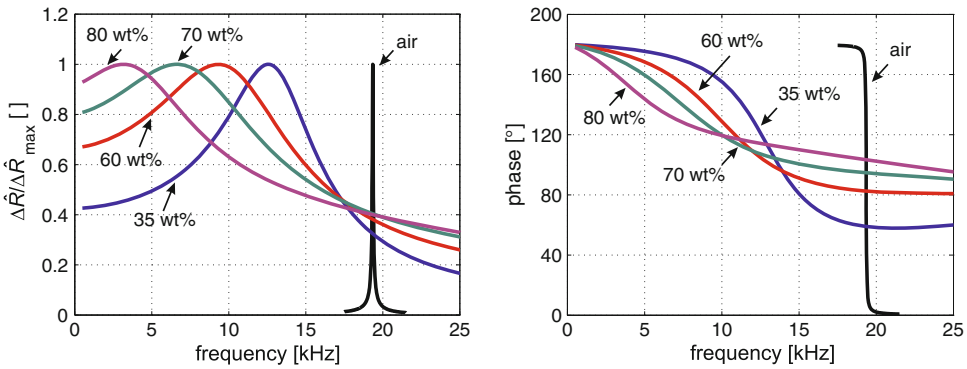

Fig. 5 Amplitude and phase of the resistance as a function of the excitation current frequency. For the simulation, air and different glycerol–water mixtures were considered

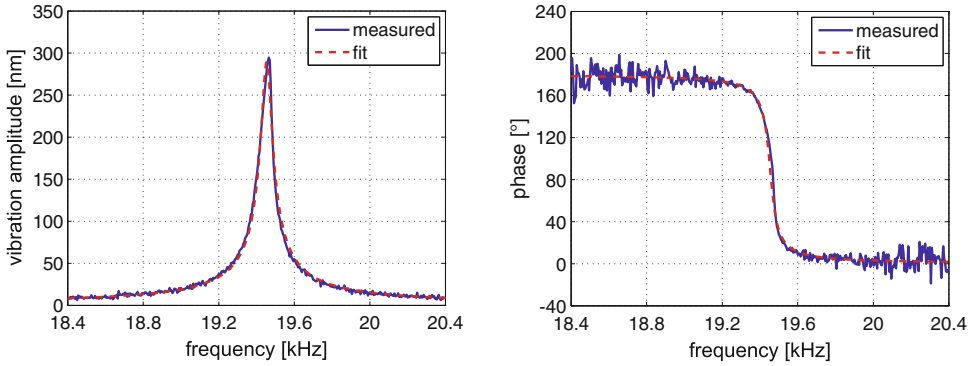

Fig. 6 Amplitude and phase of the plate deflection in air as a function of the excitation current frequency. The *dashed line* represents the fitting to a second order system

excited with a current amplitude of 20 μA whereas the magnetic field was provided by a permanent magnet of 320 mT flux density. The results of a frequency sweep measurement are depicted in Fig. 6.

The resulting vibration amplitude of the plate is in the range of several hundred nanometers. By increasing the excitation current amplitude, it is possible to reach higher values, however, non-linear spring effects like the Duffing behavior occur. In order to estimate the damping and the quality factor, we assumed that the resonant system is of second order and fitted the amplitude response

$$\hat{\psi}(f) = \left| \frac{A_0}{1 + \mathrm{j} \cdot 2D \cdot \frac{f}{f_0} - \frac{f^2}{f_0^2}} \right| \tag{7}$$

to the measured results. In the remainder of this paper, amplitudes are denoted by a "^"-symbol whereas complex-valued quantities are underlined. In Eq. (7), A_0 represents the output signal at static plate deflection ($f = 0$ Hz), D is the damping factor of the system, and f_0 is the theoretical resonant frequency of the system without damping ($f_r = f_0\sqrt{1 - 2D^2}$ is the measured resonant frequency). The fit shown in Fig. 6 was achieved for a damping value of $D = 0.001516$ with an associated quality factor $Q = 1/(2D) = 330$. The static beam deflection amounts to $A_0 = 0.88$ nm whereas the resonant frequency is $f_\mathrm{r} = 19465$ Hz which matches very well to the value of 19350 Hz predicted by the FEM simulations (Fig. 5).

6 Measurement setups

The decisive advantage of the presented sensor arises from the integrated readout based on the Wheatstone bridge circuit. The plate deflection is driven by the excitation current $i_\mathrm{e}(\mathrm{t}) = \hat{\imath}_\mathrm{e}\cos(2\pi f_\mathrm{e} t)$ whereas the bridge is supplied with the bridge voltage u_b (Fig. 1). Assuming that all bridge resistors have the same initial resistance value R_0, the resulting bridge unbalance voltage due to plate vibration is

$$\begin{aligned} u_\mathrm{d}(t) &= \frac{1}{2} u_\mathrm{b} \frac{\Delta R(t)}{R_0} = \frac{1}{2} u_\mathrm{b} \frac{\Delta \hat{R} \cos(2\pi f_\mathrm{e} t + \phi)}{R_0} \\ &= \hat{u}_\mathrm{d} \cos(2\pi f_\mathrm{e} t + \phi), \end{aligned} \tag{8}$$

where $\Delta\hat{R}$ is the maximum change of resistance of the piezoresistors and ϕ is the phase shift between the excitation current and the output signal. Since the plate vibration is driven by an AC current, it can be expected that the sensor readout will be disturbed by resistive, inductive, or capacitive crosstalk from the excitation current. There are a few possible sources for this interference. The conductive Al-layer is not protected with an isolating film and is in direct contact with the liquid. Furthermore, the excitation loop and the Wheatstone bridge use common ground connections with a resistance of approximately 3–4 Ω (Fig. 1). Depending on the chosen excitation current, the voltage drop across amounts to several mV. If both common ground connections are not equal, this voltage drop will not be canceled out by the Wheatstone bridge circuit and will therefore interfere with the sensor readout. Another important source for the signal crosstalk is a possible non-linearity of the piezoresistors which stems from the metal-semiconductor contacts. Computer models show that the nonlinear piezoresistors could cause severe interference to the sensor output (Riesch 2009). In order to achieve a sensor readout signal with minimized crosstalk, two different measurement setups were considered.

7 Measurement setup with DC bridge supply

In the first measurement setup, the bridge was supplied with a constant DC voltage of $u_\mathrm{b} = 1.5$ V. As it is not possible to fabricate completely identical piezoresistors, the sensor readout (8) contains a DC offset $u_\mathrm{d,offset}$ and can be written as

$$u_\mathrm{d}(t) = \hat{u}_\mathrm{d} \cos(2\pi f_\mathrm{e} t + \phi) + u_\mathrm{d,offset}. \tag{9}$$

Depending on the difference between initial values of the piezoresistors R_0, the offset voltage can be one order of

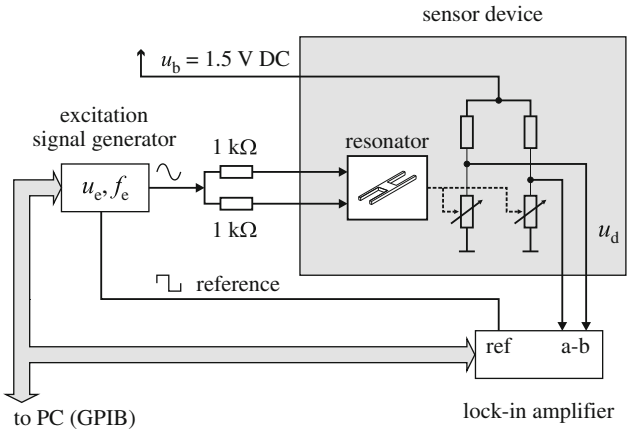

Fig. 7 Schematic diagram of the first measurement setup. The bridge was supplied with the DC voltage u_b. The amplitude of the excitation voltage $\hat{u}_e$ was set to 4.5 V_{pp} resulting in a current amplitude of 2.25 mA. The signal generator with the frequency f_e was used for both the plate excitation and the reference signal of the lock-in-amplifier

magnitude higher than the AC amplitude $\hat{u}_d$. This suggests usage of a lock-in-amplifier to extract the AC component (Fig. 7).

However, utilization of a lock-in-amplifier cannot remove the crosstalk occurring at the same frequency as the reference frequency f_e. In order to compensate for interference between excitation and readout circuits, two measurement cycles are necessary. In every cycle the frequency of the excitation signal generator is swept and the amplitude $\hat{u}_d$ and the phase ϕ are recorded. From these values, the complex amplitude of the sensor readout $\underline{\hat{u}}_d = \hat{u}_d$ $(\cos(\phi) + j \sin(\phi))$ is calculated. In the first measurement cycle we measure the output signal when a magnetic field is present (i.e., with Lorentz force excitation). This readout is our desired signal affected with the interferences. The subsequent measurement cycle is performed without the magnetic field ($B = 0$). As in this case there is no excitation, this signal represents the crosstalk only. Finally, the crosstalk-free signal can be calculated as the complex-valued difference of both outputs

$$\begin{aligned}\underline{\hat{u}}_{d,\mathrm{comp}} &= \underline{\hat{u}}_{d,\mathrm{excit}} - \underline{\hat{u}}_{d,\mathrm{noexct}} \\ &= \left(\mathrm{Re}\{\underline{\hat{u}}_{d,\mathrm{excit}}\} - \mathrm{Re}\{\underline{\hat{u}}_{d,\mathrm{noexct}}\}\right) \\ &\quad + j \cdot \left(\mathrm{Im}\{\underline{\hat{u}}_{d,\mathrm{excit}}\} - \mathrm{Im}\{\underline{\hat{u}}_{d,\mathrm{noexct}}\}\right) \\ &= \hat{u}_{\mathrm{d,comp}} e^{j\phi_{\mathrm{comp}}}. \end{aligned} \quad (10)$$

Figure 8 illustrates the compensation procedure using deionized water as sample liquid.

The compensated measurement results for several glycerol–water mixtures are depicted in Fig. 9. For these measurements, the amplitude of the excitation current was set to 2.25 mA and the magnetic field was provided by a permanent magnet of 320 mT flux density. The viscosity and the mass density of the mixtures increase with increasing mass percentage of glycerol. As a result, the damping of the plate vibrations becomes higher while the resonant frequencies and the quality factor of the system decrease.

8 Measurement setup with AC bridge supply

In order to suppress the crosstalk at the excitation frequency f_e to the sensor readout, the Wheatstone bridge can be alternatively driven with a sinusoidal voltage at the frequency f_b, i. e., $u_b(t) = \hat{u}_b \cos(2\pi f_b t)$. According to Eq. (8), the voltage of the Wheatstone bridge reads then

$$\begin{aligned} u_d(t) &= \frac{1}{2}\hat{u}_b \cos(2\pi f_b t)\frac{\Delta\hat{R}\cos(2\pi f_e t + \phi)}{R_0} \\ &= \frac{\hat{u}_b \Delta\hat{R}}{4R_0}\{\cos[2\pi(f_b - f_e)t - \phi] + \cos[2\pi(f_b + f_e)t + \phi]\}. \end{aligned} \quad (11)$$

In this case, the amplitude of the sensor readout can be obtained by setting a lock-in-amplifier to either $f_b - f_e$ or $f_b + f_e$ and consequently the interference at the excitation frequency f_e is suppressed. Figure 10 depicts the schematic of the second measurement setup.

The bridge supply frequency f_b must be at least two times higher than the maximum excitation frequency. For

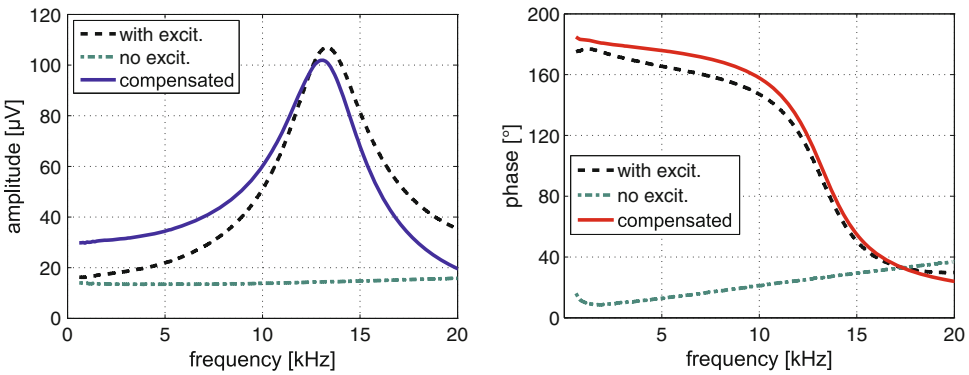

Fig. 8 Data acquiring procedure for the first setup with deionized water as sample liquid. Two measurement cycles are necessary, with (*dashed line*) and without (*dot-dashed line*) excitation. The complex-valued difference of both outputs (*solid line*) is the sensor readout compensated for crosstalk at the excitation frequency f_e

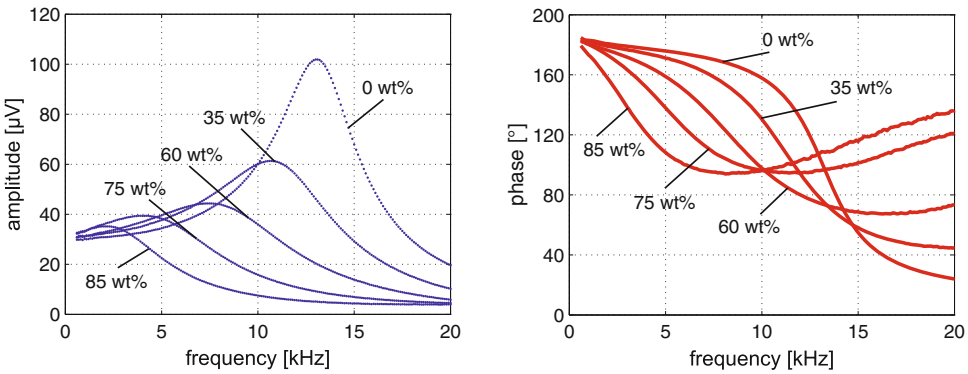

Fig. 9 Amplitude and phase of the sensor readout voltage recorded with the first measurement setup. The sensor was immersed in a variety of different glycerol–water mixtures

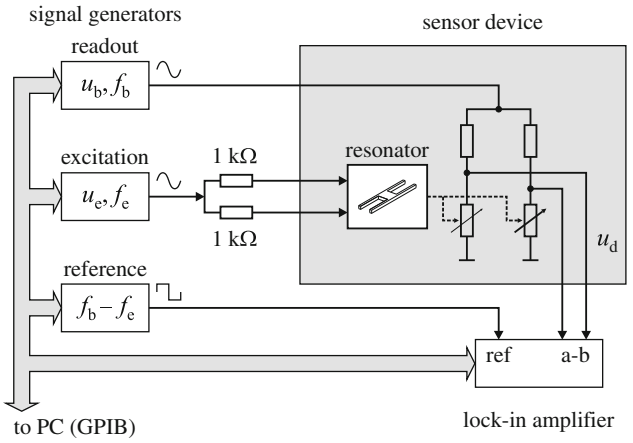

Fig. 10 Schematic diagram of the second measurement setup. The bridge was driven with a sinusoidal voltage ($f_b = 60$ kHz and $\hat{u}_b = 1.5$ V). The amplitude of the excitation $\hat{u}_e$ voltage was chosen to 4.5 V_{pp} and its frequency f_e was swept to record the output signal. The reference frequency of the lock-in-amplifier was set to $f_b - f_e$

these measurements, we set f_b to 60 kHz and $\hat{u}_b$ to 1.5 V in order to achieve comparable results with the first measurement setup. Again, the magnetic field was established utilizing the permanent magnet of 320 mT flux density and the excitation current amounts to 2.25 mA. Figure 11 illustrates the results obtained for the same glycerol–water concentrations. The comparison between Fig. 9 and Fig. 11 as well as Eq. (8) (for $u_b = \text{const}$) and Eq. (11) reveals that the amplitude of the sensor readout in the second case is reduced by half because only one sideband of the bridge unbalance voltage u_d is used to acquire the sensor readout. Moreover, since we utilized the difference $f_b - f_e$ as reference frequency for the Lock-in-amplifier, the phase of the sensor readout is mirrored on the frequency axis (owing to the $-\phi$ term in Eq. (11)).

9 Measurement results

The liquid viscosity is highly temperature dependent. Thus, the sample temperature must be kept constant in order to obtain reproducible results. For all measurements we used a small cooper container equipped with a Peltier-element and a temperature sensor. A temperature controller maintained a constant container temperature of 25°C. We filled the chamber with a liquid probe of approximately 1 ml. In order to minimize spurious readout effects associated to temperature gradients, a rest time of at least 15 minutes was awaited before further measurement steps were carried out. The following analysis of the data is related to the first measurement setup. As the measured characteristics recorded with the second setup exhibit the same trend, the analogous post-processing procedure yields equivalent results.

The liquid composition influences the vibration behavior of the system. With an increasing percentage of glycerol, the resonant frequency and the quality factor of the system decrease. Recording these parameters enables simultaneous measurement of viscosity and density of the mixture. However, whereas the resonant frequency can be measured directly, the quality factor, or equivalently the damping of the system, must be estimated by fitting the amplitude of the second order system (7) to the measured results. Figure 12 shows as an example the fitting result for 60 wt% glycerol–water mixture. Another useful characteristic parameter is the inflection point of the phase characteristic. The related characteristic frequency f_{ch} is slightly higher than f_r and can be obtained by calculating a second derivate of the phase characteristic.

Table 1 summarizes parameters of the liquids and measurement results. Glycerol mixtures with up to 80 mPas of dynamic viscosity were investigated. Higher values cause a resonant shift to very low frequencies resulting in a deterioration of the damping factor estimation.

The measured data and the corresponding fit equations are plotted in Fig. 13. For reasons of clarity, the plot of characteristic frequency f_{ch} was omitted. This characteristic has the same trend as the resonant frequency f_r and can be used instead. However, due to the second derivate calculation, the obtained relative error is higher. The concentration of glycerol in the mixture c_{glyc} (in weight %) can be

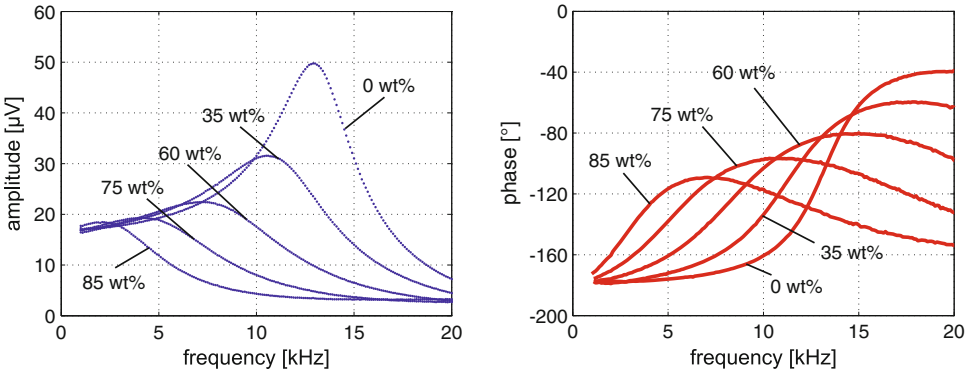

Fig. 11 Amplitude and phase of the sensor readout recorded with the second measurement setup. The sensor was immersed in a variety of glycerol–water mixtures. In comparison to Fig. 9, the amplitude of the sensor readout is halved and the phase is mirrored on the frequency axis

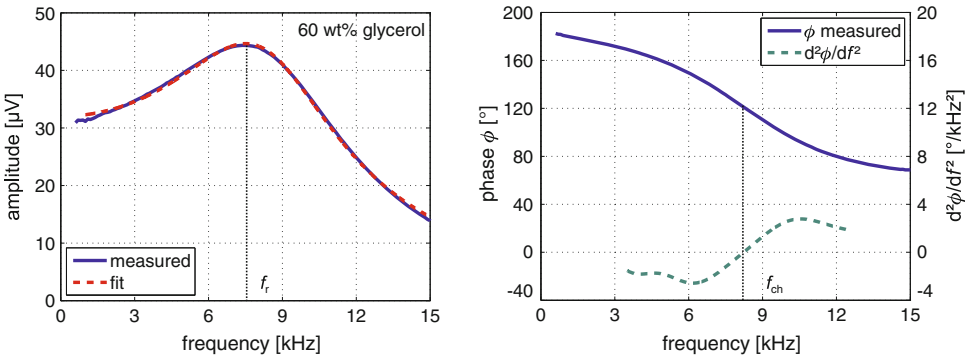

Fig. 12 Frequency sweep measurement of the sensor output voltage (*solid line*). The *dashed line* (subfigure left) represents a second-order system fit used to estimate the damping factor D. At f_r, the amplitude reaches its maximum. Another characteristic parameter is the frequency f_{ch} where the inflection point of the phase characteristic occurs (*dashed line*, subfigure right)

Table 1 Evaluation of the measurement data for used glycerol–water mixtures

Glycerol (wt%)	η[a] (mPas)	ρ[b] (kg/m^3)	D (–)	f_r (Hz)	f_{ch} (Hz)
0	0.89	997.1	0.144	13,066	13,286
20	1.54	1,045.3	0.188	12,040	12,412
35	2.6	1,083.9	0.254	10,670	11,260
50	5.04	1,123.8	0.323	9,114	9,841
60	8.82	1,151.1	0.39	7,436	8,294
65	12.36	1,164.8	0.43	6,416	7,407
70	17.96	1,178.4	0.466	5,304	6,000
75	27.73	1,192	0.509	4,140	4,998
80	45.86	1,205.5	0.552	3,054	3,831
83	64.2	1,213.4	0.574	2,479	3,213
85	81.5	1,218.7	0.592	2,126	2,770

[a] Sheely 1932

[b] Bosart and Snoddy 1928

well fitted for both output parameters by a third-order polynomial function.

In practice, first the frequency sweep measurement must be performed and the resonant frequency as well as the damping calculated. After estimating the glycerol percentage using the fit equations, the look-up tables (Sheely 1932; Bosart and Snoddy 1928) are applied to obtain the viscosity and the mass density of the mixture. In order to verify the feasibility of this approach, we compared the rated values with the measurement results (Table 1). The highest absolute error for c_{glyc} amounts to 2 wt%. Applying look-up tables, the viscosity of the mixture can be estimated with an accuracy better than 10% whereas the relative error for mass density lies far below 1%.

In many industrial applications, the change of the viscosity rather than its absolute value is of particular importance (e.g., monitoring and controlling of process flows). Thus, the sensor is best suitable for online monitoring systems as the variations of the resonant frequency can be fast and accurately evaluated.

In comparison to the measurement results, Fig. 13 illustrates also the results obtained by FEM simulations. Whereas the trend of both characteristics is similar to the measured ones, the absolute values reveal the maximum deviation of about 25% for resonant frequency and 15% for damping factor. The reason for that are numerous simplifications made by sensor modeling. Since the plate damping was totally neglected, the simulations yield a smaller damping factor in the lower viscosity range as measured. For precise modeling of the piezoresistive elements, the stress tensor and the piezoresistance matrix of silicon must be utilized over the whole volume of the piezoresistor, whereas we just used the longitudinal stress σ_l according to Eq. (6). Neither the measured sensor output nor the simulated one can be exactly described by the system of second order as assumed for the fitting procedure (Eq. (7)) in order to obtain the damping factor D. This mismatch increases

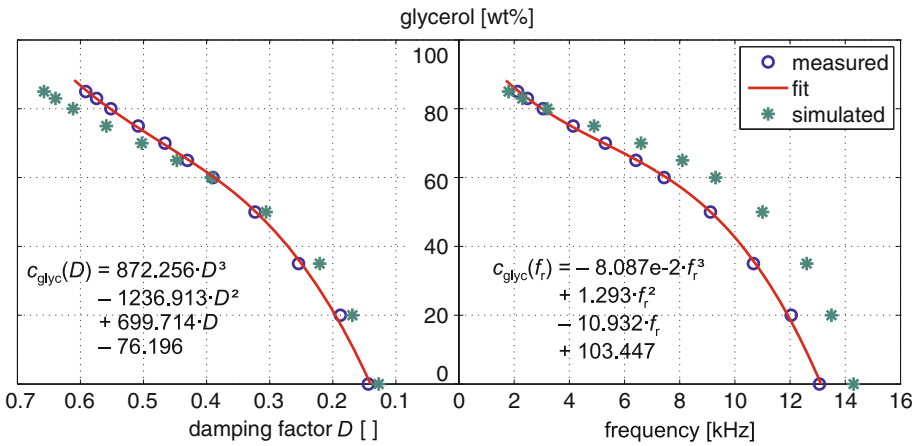

Fig. 13 Plot of the measured data summarized in Table 1 with corresponding fit functions. For the concentration of glycerol in mixture c_{glyc}, a polynomial fit was used. The *stars* represent the results predicted by FEM simulations

with higher damping factor. Therefore, for high glycerol percentage only the narrow frequency range up to double resonant frequency was used for the fitting. Due to said simplification by the modeling of the piezoresistors, the deviations from the second-order system are more emphasized by simulation results. This can explain the change of the trend of the simulated characteristic in the higher viscosity range. The influence of the ambient temperature (25°C) was only considered regarding the viscosity and density of the liquid under the test, whereas its impact on the mechanical properties of the sensor materials was neglected. Moreover, the possible intrinsic stress of the vibrating structure was not analyzed. Taking into account all these effects may shift the simulated resonant frequency to lower values yielding a better agreement with the measurement results.

Nevertheless, the simulation results are accurate enough to get a glimpse of the trend of the output characteristics and to roughly estimate the resonant frequency and the damping. Moreover, the described simulation model is suitable to qualitatively investigate the impact of the geometry variations on the sensor output which is of great importance to sensor design.

10 Summary and conclusion

A resonant MEMS sensor suitable for monitoring of viscosity and mass density of liquids was presented. The core sensing element of the device is a rectangular, in-plane vibrating plate suspended by four beam springs which is damped by the liquid under test. The decisive advantage of this layout is the integrated piezoresistive readout based on the Wheatstone bridge.

A simulation approach that combines analytical and numerical modeling was introduced. The simulation results give the right trend of output characteristics for varied viscosity and help to estimate the resonant frequency and the damping. The model is also useful for the sensor design, as the effects of geometry variations can be studied qualitatively.

For experimental characterization of the sensor, two different operating modes of the readout were considered. In the first mode the bridge is driven by a DC voltage. The frequency of the excitation current is swept and a lock-in-amplifier is used to separate the bridge output from the DC offset which arises from the difference in initial values of the piezoresistors. In this mode, two sweep cycles are necessary, with and without the magnetic field. The results without the Lorentz force excitation (i.e., magnetic field) are used to compensate for interference caused by various coupling mechanisms between excitation and readout circuits. Alternatively, the bridge can be driven by a sinusoidal voltage. In this case, the plate deflection is obtained by setting the lock-in-amplifier reference to the difference of the excitation and the bridge frequency. This eliminates the crosstalk and the need for an additional measurement cycle, however, at the expense of higher measurement setup complexity and lower amplitudes of the sensor readout.

The sensor was tested using glycerol–water mixtures at constant temperature. As characteristic properties of the resonant system, the damping factor and the resonant frequency were evaluated. Generally, these parameters are a complex function of both viscosity and density. However, for glycerol–water mixtures, simple fit functions for glycerol percentage in mixture were found. Applying look-up tables allows precise estimation of viscosity and mass density of the mixture under test. The sensor is particularly suitable for online monitoring systems where only the variations of the resonant frequency are of importance.

Acknowledgments We gratefully acknowledge financial support by the Austrian Science Fund (FWF): L657-N16. The authors would also like to thank Dr. Artur Jachimowicz (Institute of Sensor and Actuator Systems, Vienna University of Technology) and Dr. Peter Hudek (Research Centre for Microtechnology, Vorarlberg University of

Applied Sciences) for their support on the fabrication of the sensor device.

References

Beigelbeck R, Jakoby B (2004) A two-dimensional analysis of spurious compressional wave excitation by thickness-shear-mode resonators. J Appl Phys 95(9):4989–4995. doi: 10.1063/1.1697637

Beigelbeck R, Nachtnebel H, Kohl F, Jakoby B (2011) A novel measurement method for the thermal properties of liquids by utilizing a bridge-based micromachined sensor. Meas Sci Technol 22(10):105407. doi:10.1088/0957-0233/22/10/105407

Bosart LW, Snoddy AO (1928) Specific gravity of glycerol. Ind Eng Chem. 20:1377–1379. doi: 10.1021/ie50228a032

Grob RL, Barry EF (2004) Modern practice of gas chromatography. Wiley, New York

Hopcroft MA, Nix WD, Kenny TW (2010) What is the Young's modulus of silicon? J Microelectromechanical Syst 19(2):229–238. doi: 10.1109/JMEMS.2009.2039697

Jakoby B (2008) Efficient semi-numerical analysis of acoustic sensors using spectral domain methods—a review. Meas Sci Technol 19:1–14. doi:10.1088/0957-0233/19/5/052001

Jakoby B, Vellekoop MJ (2004) Physical sensors for water-in-oil emulsions. Sens Actuators A 110(1–3):28–32. doi: 10.1016/j.sna.2003.08.005

Kanazawa KK, Gordon JG (1985) Frequency of a quartz microbalance in contact with liquid. Anal Chem 57:1770–1771. doi: 10.1021/ac00285a062

Kuntner J (2008) Oil Condition Monitoring Using Physical Chemosensors. Vienna University of Technology, Dissertation

Kuntner J, Kohl F, Jakoby B (2006) Simultaneous thermal conductivity and diffusivity sensing in liquids using a micromachined device. Sens Actuators A 130–131:62–67. doi: 10.1016/j.sna.2005.11.021

Lucklum F, Jakoby B (2008) Novel magnetic–acoustic resonator sensors for remote liquid phase measurement and mass detection. Sens Actuators A 145–146:44–51. doi:10.1016/j.sna.2007.10.031

Martin SJ, Granstaff VE, Frye GC (1991) Characterization of a quartz crystal microbalance with simultaneous mass and liquid loading. Anal Chem 63(20):2272–2281. doi:10.1021/ac00020a015

Nabil A, Diego FN, Vincent TM (2001) Measurement of solution viscosity by atomic force microscopy. Rev Sci Instrum 72:2731–2734. doi:10.1063/1.1368856

Reichel EK, Riesch C, Weiss B, Jakoby B (2008) A vibrating membrane rheometer utilizing electromagnetic excitation. Sens Actuators A 145–146:349–353. doi:10.1016/j.sna.2007.10.056

Reichel EK, Riesch C, Keplinger F, Jakoby B (2009) Modeling of the fluid-structure interaction in a fluidic sensor cell. Sens Actuators A 156:222–228. doi:10.1016/j.sna.2009.03.002

Riesch C (2009) Micromachined viscosity sensors. Shaker Verlag, Aachen

Riesch C, Jachimowicz A, Keplinger F, Reichel E K, Jakoby B (2007) A novel sensor system for liquid properties based on a micromachined beam and a low-cost optical readout. Proc IEEE Sens Conf Atlanta USA. doi:10.1109/ICSENS.2007.4388540

Riesch C, Reichel E K, Jachimowicz A, Keplinger F, Jakoby B (2008) A micromachined doubly-clamped beam rheometer for the measurement of viscosity and concentration of silicon-dioxide-in-water suspensions. Proc IEEE Sens Conf Lecce Italy. doi: 10.1109/ICSENS.2008.4716461

Sader JE (1998) Frequency response of cantilever beams immersed in viscous fluids with applications to the atomic force microscope. J Appl Phys 84:64–76. doi:10.1063/1.368002

Sheely ML (1932) Glycerol viscosity tables. Ind Eng Chem 24:1060–1064. doi: 10.1021/ie50273a022

Shi TM, Xie CG, Huang SM, Williams RA, Beck MS (1991) Capacitance-based instrumentation for multi-interface level measurement. Meas Sci Technol 2:923–933. doi: 10.1088/0957-0233/2/10/006

Toth FN, Meijer GCM, van der Lee M (1997) A planar capacitive precision gauge for liquid-level and leakage detection. Trans Instrum Meas 46(2):644–646. doi: 10.1109/19.572052

Viswanath DS, Ghosh TK, Prasad DHL, Dutt NVK, Rani KY (2007) Viscosity of liquids. Springer, Berlin